Industrial Chemistry & Materials

ROYAL SOCIETY OF CHEMISTRY

PAPER

View Article Online
View Journal

Check for updates

Cite this: DOI: 10.1039/d5im00204d

Synergistically engineered B- and P-doped graphite felts as tailored asymmetric electrodes for aqueous quinone-based redox flow batteries

Minghua Jing,[a] Yanqiu Chen,[b] Yuxuan Yang,*[b] Mengnan Zhang,[b] Bo Wang,[b] Zeyu Xu*[c] and Dawei Fang *[a]

Aqueous organic redox flow batteries (AORFBs) have emerged as a novel type of large-scale, long-duration energy storage technology, garnering significant attention due to their resource and cost benefits. However, the electrode reaction kinetics of various electroactive substances differ fundamentally. Consequently, it is essential to design electrode materials that are tailored to specific organic electroactive substances to enhance the performance of AORFBs even further. This study investigates the composition and structural characteristics of various heteroatom-doped graphite felt (GF) electrode materials and their electrochemical reactivity towards the positive benzoquinone disulfonic acid ($BQDSH_2$) and negative anthraquinone sulfonic acid (AQSH) electrolytes. Several patterns and insights are deduced. Among pristine graphene (GF) and five heteroatom-doped graphenes (N, O, P, B, S), B-doped GF and P-doped GF exhibit the best electrochemical activity for $BQDSH_2$ and AQSH, respectively. Density functional theory has confirmed that electrodes with different properties exhibit distinct characteristic reactivities towards various electroactive substances. The effectiveness of designing the positive and negative electrodes separately to enhance the performance of AORFBs is further verified through kinetic tests and the assembly of asymmetric batteries. By conducting targeted design for the positive and negative electrodes, the energy efficiency and utilization rate of the all-quinone AORFBs has increased by 18% and 10%, and the power density has risen by nearly 43%. All these results have verified the effectiveness and necessity of the targeted design of electrode materials in improving the performance of AORFBs.

Received 15th August 2025,
Accepted 16th September 2025

DOI: 10.1039/d5im00204d

rsc.li/icm

Keywords: AORFBs; Quinone; Graphite felt; Heterogeneous electrode; Heteroatom-doped.

1 Introduction

As the large consumption of primary fossil energy has caused serious environmental pollution, renewable energy is set to become the main source of energy. However, its intermittency and the mismatch between supply and demand limit its large-scale utilization.[1–3] Developing new energy storage equipment to realize the efficient use of clean energy has become the trend of the times. Electrochemical energy storage has been widely used due to its high energy density, strong adjustability, fast response speed, and many other advantages. The capacity and power units of aqueous redox flow batteries (ARFBs) are independent of each other, and they are inherently safe, making them one of the most promising options for large-scale, long-duration energy storage.[4–7] All-vanadium redox flow batteries (VRFBs) represent the most mature form of ARFB energy storage technology.[8,9] Nonetheless, because of the restricted availability of vanadium resources and the elevated cost of vanadium electrolytes, there is an imperative to develop alternative, more affordable ARFB systems. Aqueous organic redox flow batteries (AORFBs) use water-soluble organic electroactive materials as their energy carrier. The raw electrolyte materials for these batteries are readily available, and their performance can be flexibly adjusted, making them one of the most highly regarded types of new ARFBs.[10–12]

The organic active electrolytes of AORFBs that have been studied extensively include quinones,[13] azobenzene,[14] 2,2,6,6-tetramethyl-1-piperidinyloxy (TEMPO),[15] viologens (Vi),[16] ferrocenes,[17] and phenazines.[18] Quinone derivatives exhibit a rapid two-electron reaction, making them the earliest and most widely used organic active electrolytes, applicable in acidic, alkaline, and neutral environments.[19,20] Aziz[21] initially

[a] Institute of Rare and Scattered Elements, Liaoning University, Shenyang, 110036, China. E-mail: dwfang@lnu.edu.cn
[b] College of Chemistry, Liaoning University, Shenyang, 110036, China. E-mail: yangyuxuan@lnu.edu.cn
[c] State Key Laboratory of Materials Low-Carbon Recycling and Department of Chemical Engineering, Beijing University of Technology, Beijing 100124, China. E-mail: ze-yu.xu@bjut.edu.cn

constructed a metal-free flow battery utilizing 9,10-anthraquinone-2,7-disulfonic acid ($AQDSH_2$) as the negative electrolyte, Br_2/Br^- as the positive electrolyte, and inexpensive carbon electrodes. The peak galvanic power density of this battery exceeded 0.6 W cm^{-2} at a current density of 1.3 A cm^{-2}, and the storage capacity retention per cycle was 99%. Since then, an increasing number of researchers have focused on quinone-based AORFBs and have dedicated themselves to the development of new and highly efficient aqueous organic electrolytes. Yang[22] utilized 9,10-anthraquinone-2-disulfonic acid (AQSH) and 1,2-dihydroxy-3,5-benzene disulfonic acid ($BQDSH_2$) as a redox-active couple, along with carbon paper coated with carbon black as the electrode, to assemble an all-quinone AORFB. The capacity at 10 mA cm^{-2} was over 90% of the theoretical capacity. The use of a carbon paper electrode created a barrier to convective transport, resulting in a diffusion layer thickness of 150 microns. This reduced the limiting current density and decreased the cell voltage. Zhang[23] selected 3,4-dihydroxy-9,10-anthraquinone-2-sulfonic acid (ARSH) as the negative active material and $BQDSH_2$ as the positive active material, using carbon paper as the electrode to construct an all-quinone AORFB. The energy efficiency of this battery was below 40%, a result of the low solubility of ARSH and the carbon paper electrode.

Despite the development of numerous organic electrolytes for AORFBs, research into the corresponding electrode materials is relatively scarce. This, to some extent, restricts the performance of the batteries, as the electrodes significantly influence the performance of AORFBs. Graphite felt (GF) electrodes are the most widely used in ARFBs[24,25] due to their high conductivity, corrosion resistance and large specific surface area, which are provided by the three-dimensional porous structure. Since the hydrophilicity and electrochemical activity of the original GF are unsatisfactory, it is necessary to modify the GF electrode to enhance battery performance.[26–28] Traditional treatment of GF electrode includes acid treatment,[29] heat treatment,[30] electrochemical oxidation[31] and catalyst modification,[32,33] which can provide more active sites for the electrochemical redox reactions. Compared to the catalyst modification strategy, surface heteroatom-doping[34–36] of electrode materials is better suited for the actual application conditions of RFBs, where the electrolyte continuously scours the electrodes during operation.

Zhao[37] reported on an ultra-stable boron-doped graphite felt (B–GF) electrode featuring highly active reaction sites, demonstrating higher energy efficiency and exceptional stability over long-term cycling tests when applied in VRFBs. Lee[38] prepared a GF electrode with dual-doping of nitrogen and oxygen for VRFBs by subjecting it to oxidative thermal treatment with urea and polyethylene glycol (PEG). The dual-doping GF electrode helps to reduce cell polarization and significantly enhances the energy efficiency and charge–discharge capacities of VRFBs. Su[39] presented a phosphorus-doped graphite felt (P–C_3N_4@GF) electrode, created through a simple and environmentally friendly method using melamine and 1-hydroxyethylidene-1,1-diphosphonic acid (HEDP). This electrode demonstrated exceptional rate performance and superior stability in VRFBs. Roth[40] utilized pyrrole-2-carboxaldehyde and 2-thiophenecarboxaldehyde as sources of nitrogen and sulfur, respectively, to synthesize a porous N- and S-doped PAN-based carbon felt. This material exhibited promising activity for the positive reaction of VRFBs. Clearly, at present, the majority of GF electrode modifications are

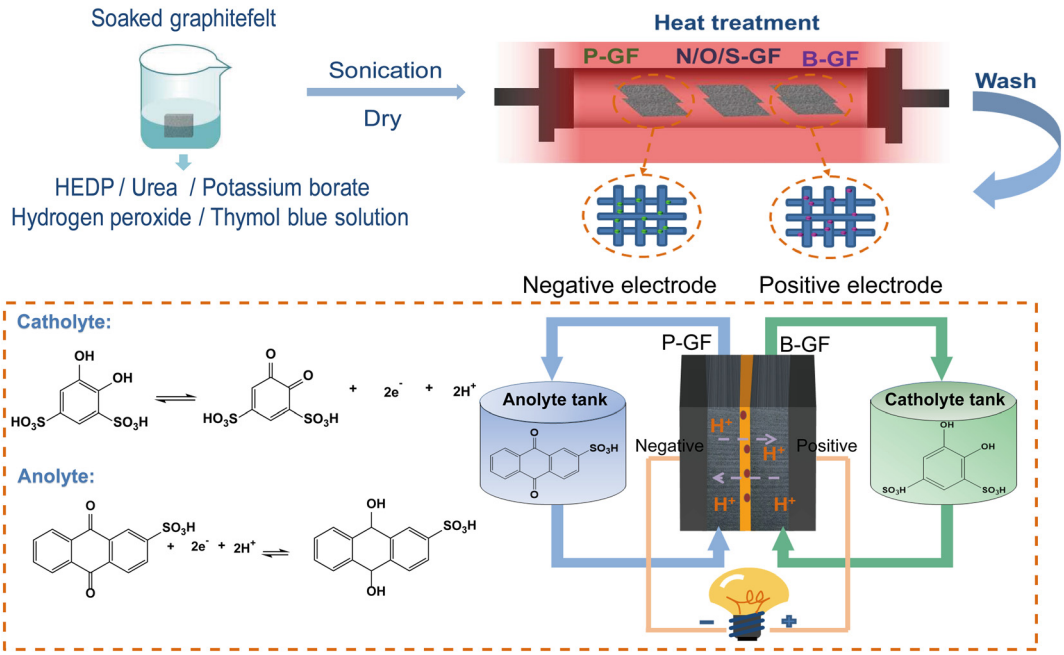

Scheme 1 Preparation process of heteroatom-doped GF materials and application of P–GF and B–GF in all quinone-based AORFBs.

aimed at VRFBs. Since different active electrolytes possess inherently distinct electrochemical reaction kinetics, the performance criteria for electrode materials will differ accordingly. Nevertheless, the development of specialized electrode materials for AORFBs remains quite limited at this time.

In this paper, GFs doped with N, S, P, O, and B have been prepared by simple soaking and high-temperature calcination. The electrochemical reaction activities of $BQDSH_2$ and AQSH on various electrode materials were investigated systematically. The surface composition and microstructure of the electrode materials were characterized. Through electrochemical tests and DFT calculations, B–GF and P–GF materials were identified as the most suitable electrodes for the $BQDSH_2$ and AQSH electrolytes, respectively. The preparation processes were further optimized. AQSH, as the negative active substance, $BQDSH_2$, as the positive active substance, P–GF and B–GF as the negative and positive electrodes, respectively, were used to assemble an all-quinone AORFB (Scheme 1). The battery demonstrated excellent performance and stability compared to that equipped with pristine GF electrodes. The coordinating wettability, conductivity and specific catalytic activity of electrodes may be key factors in enhancing battery performance. This work presents a research approach for the design and modification strategy of electrodes for AORFBs.

2 Results and discussion

Firstly, the electrochemical activity of AQSH and $BQDSH_2$ electrolytes on various heteroatom-doped GF and original GF has been studied using cyclic voltammetry, with the results shown in Fig. 1a and b. As depicted in Fig. 1a, all the activated GFs showed superior reactivity towards AQSH. Among all electrodes doped with heteroatoms, P–GF exhibited the highest peak current and the smallest peak potential difference without ohmic compensation. This suggests that the P–GF material possesses superior electrocatalytic activity for AQSH. Regarding the positive electrode $BQDSH_2$, as illustrated in Fig. 1b, the situation is more intricate than that of the negative AQSH. Most heteroatom-doped electrodes exhibit even lower electrochemical activity for $BQDSH_2$ compared to the pristine GF. Only B-doped electrodes demonstrate enhanced activity for it, which may be attributed to its relatively rapid electrode reaction kinetics. Introducing excessive heteroatoms and compromising electron conduction performance could further impede the reaction process.

Besides, the electrochemical impedance spectra and corresponding fitting data for AQSH and $BQDSH_2$ at potentials of −0.13 V and 0.658 V, respectively, are presented in Fig. S1. The two semi-cycles represent the interface resistance (R_c) and charge transfer resistance (R_{ct}), the line indicates the diffusion process, and R_s corresponds to the solution resistance. This suggests that the process is under mixed control, involving both charge transfer and diffusion. Among the materials tested, AQSH on P–GF and $BQDSH_2$ on B–GF exhibited the lowest resistance values. P–GF and B–GF exhibit superior electrochemical activity for AQSH and $BQDSH_2$, making them more suitable for quinone-based AORFBs. The results above indicate that the various electrode surfaces and structural characteristics have distinct effects on the reactions of different electroactive substances. This further validates the necessity of designing the composition and structural characteristics of electrode materials based on the kinetics of various electrode reactions.

The processing technique significantly affects the surface composition and microstructure of the electrode material. Building upon the aforementioned electrochemical research findings, the impact of preparation conditions on the electrochemical performance of P–GF and B–GF materials was further explored by electrochemical tests to further enhance the performance of the electrodes. Fig. 1c–e present the CV profiles of P–GF prepared under various conditions, including the concentration of HEDP, calcination temperature, and soaking durations. Among the electrode materials prepared at different immersion concentrations, the electrode materials prepared at 0.4 M HEDP exhibited the largest peak current and the smallest redox peak difference. If the concentration of HEDP is too low, it will result in insufficient introduction of active sites; conversely, if the concentration is too high, it may lead to a loss of electron transport performance. This indicates that an immersion concentration of 0.4 M HEDP is optimal. During the study of calcination temperatures, it was noted that the peak redox current of AQSH on the electrode material prepared at 900 °C with a 3 hour dwell time was higher, and the difference in peak position was minimal without ohmic compensation. This suggests that the electrochemical reaction of the active material AQSH on the P–GF-0.4-900-3 h electrode material demonstrated optimal reversibility and activity, potentially due to the synergistic effects of active sites and electrical conductivity.

Fig. 1f–h display the cyclic voltammetry (CV) curves of $BQDSH_2$ on B–GF, prepared using varying concentrations of $K_2B_4O_7$, different calcination temperatures, and various holding times. During the optimization of the $K_2B_4O_7$ concentration (refer to Fig. 1f), it was observed that the peak current in the CV curves of $BQDSH_2$ on B–GF increased notably as the concentration rose from 0.12 M to 0.36 M. Nevertheless, when compared to the material produced using a 0.36 M $K_2B_4O_7$ solution, the activity of the material from a 0.48 M immersion solution was marginally inferior. This suggests that the concentration of the boron source has a considerable impact on the material's activity. The optimization of the calcination temperature (Fig. 1g) revealed that $BQDSH_2$ on B–GF, prepared at 900 °C, exhibited the highest redox peak current and the smallest peak position difference among the materials. In the optimization of the holding time (Fig. 1h), it was observed that the reversibility of the material prepared with an excessively long holding time (7 hours) was very poor,

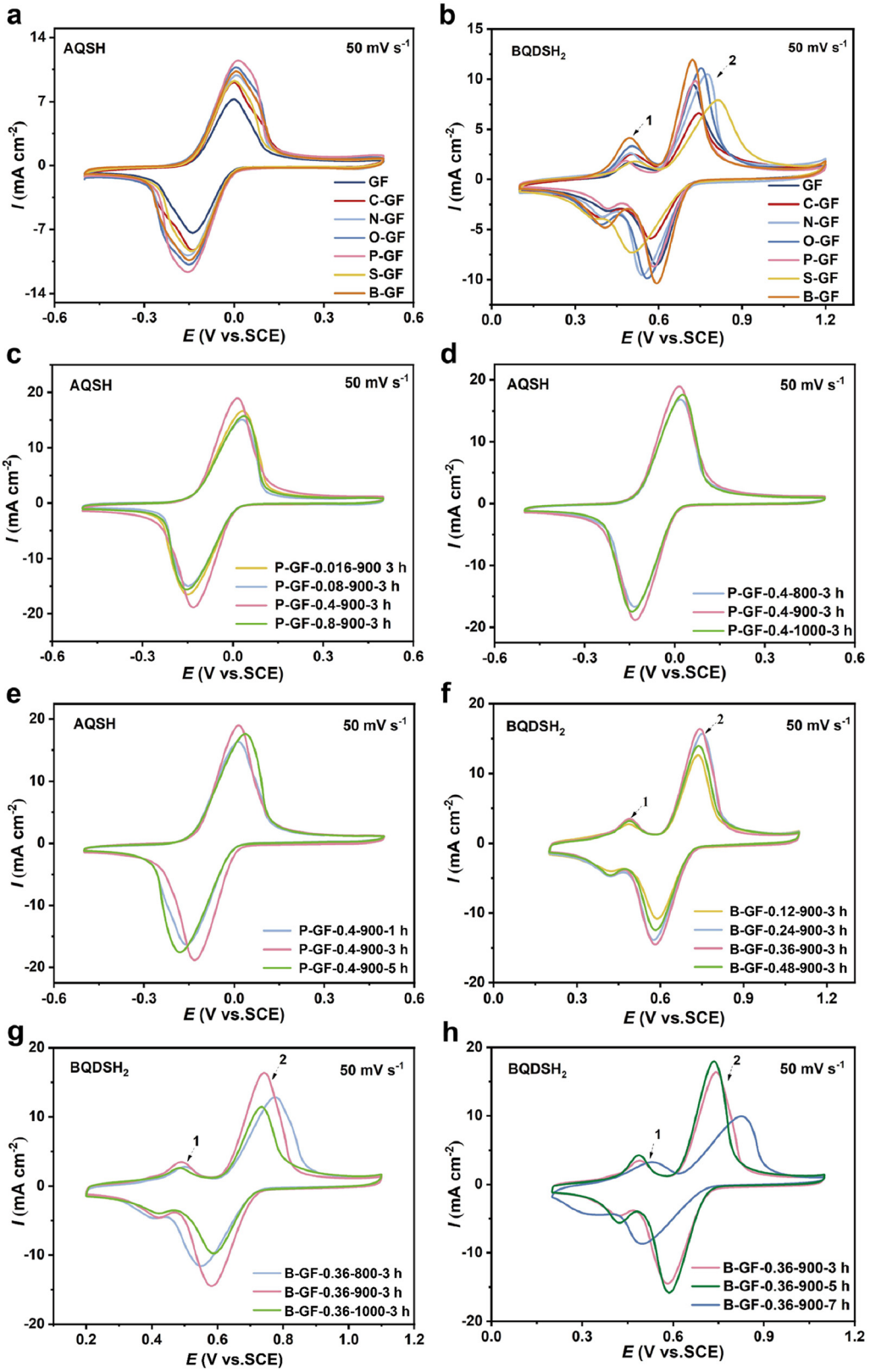

Fig. 1 CV curves of heteroatom-doped GF in 5 mM AQSH (a) and 5 mM $BQDSH_2$ (b); CV curves of P–GF prepared under various concentrations of HEDP (c), at different calcination temperatures (d) and at different holding temperatures in 5 mM AQSH (e); CV curves of B–GF prepared under various concentrations of $K_2B_4O_7$ (f), at different calcination temperatures (g) and at different holding temperatures in 5 mM $BQDSH_2$ (h).

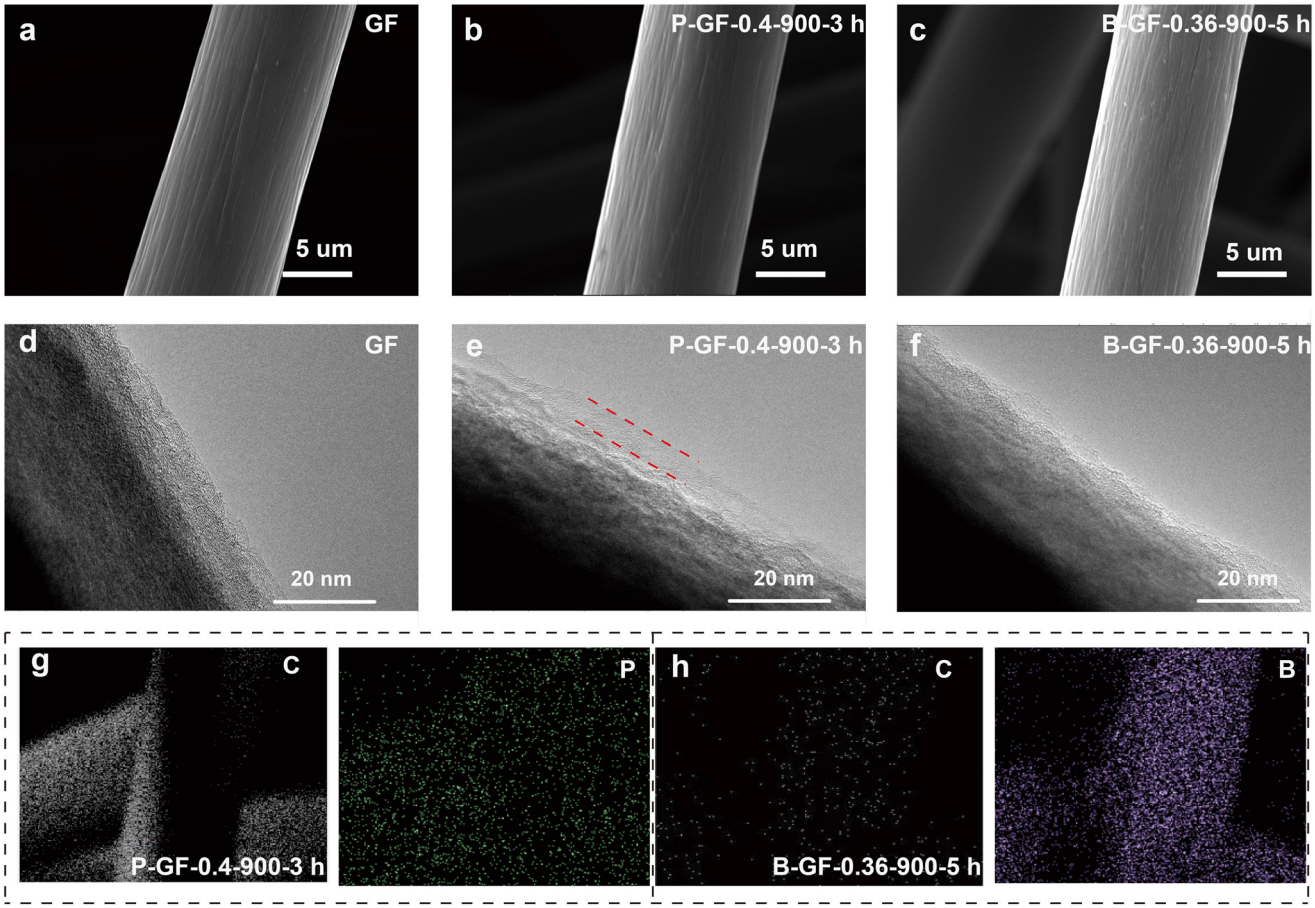

Fig. 2 SEM images of GF (a), P–GF (b) and B–GF (c); TEM images of GF (d), P–GF (e) and B–GF (f); EDS mapping of P–GF (g) and B–GF (h).

indicating that prolonged carbonization times were detrimental to maintaining the activity of the material against $BQDSH_2$. In summary, for the electrochemical reaction of $BQDSH_2$, the electrode material activity was optimal for the sample prepared through immersion in 0.36 M $K_2B_4O_7$ and calcination at 900 °C for 5 hours.

The microstructures of GF, P–GF, and B–GF prepared under the optimal preparation conditions are shown in Fig. 2. Fig. 2a–c indicate that the fiber diameter of the three electrode materials is approximately 10 μm. Following heteroatom doping modification, the fiber size remains largely unchanged; however, the microscopic morphology of the fiber surface exhibits distinct differences (Fig. 2d–f). Compared to the pristine GF, the P–GF fiber surface features a thin carbon layer, which may be attributed to the thermal decomposition and deposition of HEDP organic molecules in a high-temperature inert atmosphere. This could be more beneficial for enhancing activity and conductivity (Fig. 2d and e). The surface of the B–GF material is quite rough and exhibits numerous defects (Fig. 2f), which may be attributed to the etching effect of potassium tetraborate on it. An increased number of defects can contribute to providing additional reactive sites, thus facilitating the progression of electrochemical reactions. The EDS mapping of P–GF and B–GF confirmed the existence of P and B elements on the fiber surface, indicating the successful and uniform doping of P and B (Fig. 2g and h). And the surface element contents of B and P in B–GF and P–GF are 2.2% and 0.9%, respectively. Based on the results of the CV test, there are significant differences in the electrochemical reaction kinetics between AQDS and BQDS. The surface characteristics of the electrode materials must be tailored to the specific requirements of different electrochemical reactions.

The contact angle test results are presented in Fig. 3a–c. The B- and P-doped GFs exhibited superior infiltration compared to the pristine GF, suggesting that the heteroatom doping process may enhance the contact between the electrode and electrolyte, thereby improving the electrochemical surface area. The contact angle of B–GF was smaller than that of P–GF, which may be attributed to the greater number of defects in B–GF. The CV tests at different scan rates for GF, P–GF, and B–GF in 1 M H_2SO_4 are depicted in Fig. 3d–f. A linear relationship between the current and scan rate was established, from which the electrochemical active surface area (ECSA) can be calculated using the slope (eqn (S1) and (S2))[41] as illustrated in Fig. 3g. The ECSAs of P–GF and B–GF were larger than that of GF obviously. And the increase in the ECSA of B–GF and P–GF compared to GF is similar to that of the BET specific surface area (Fig. 3h and i). This indicates that after the modification

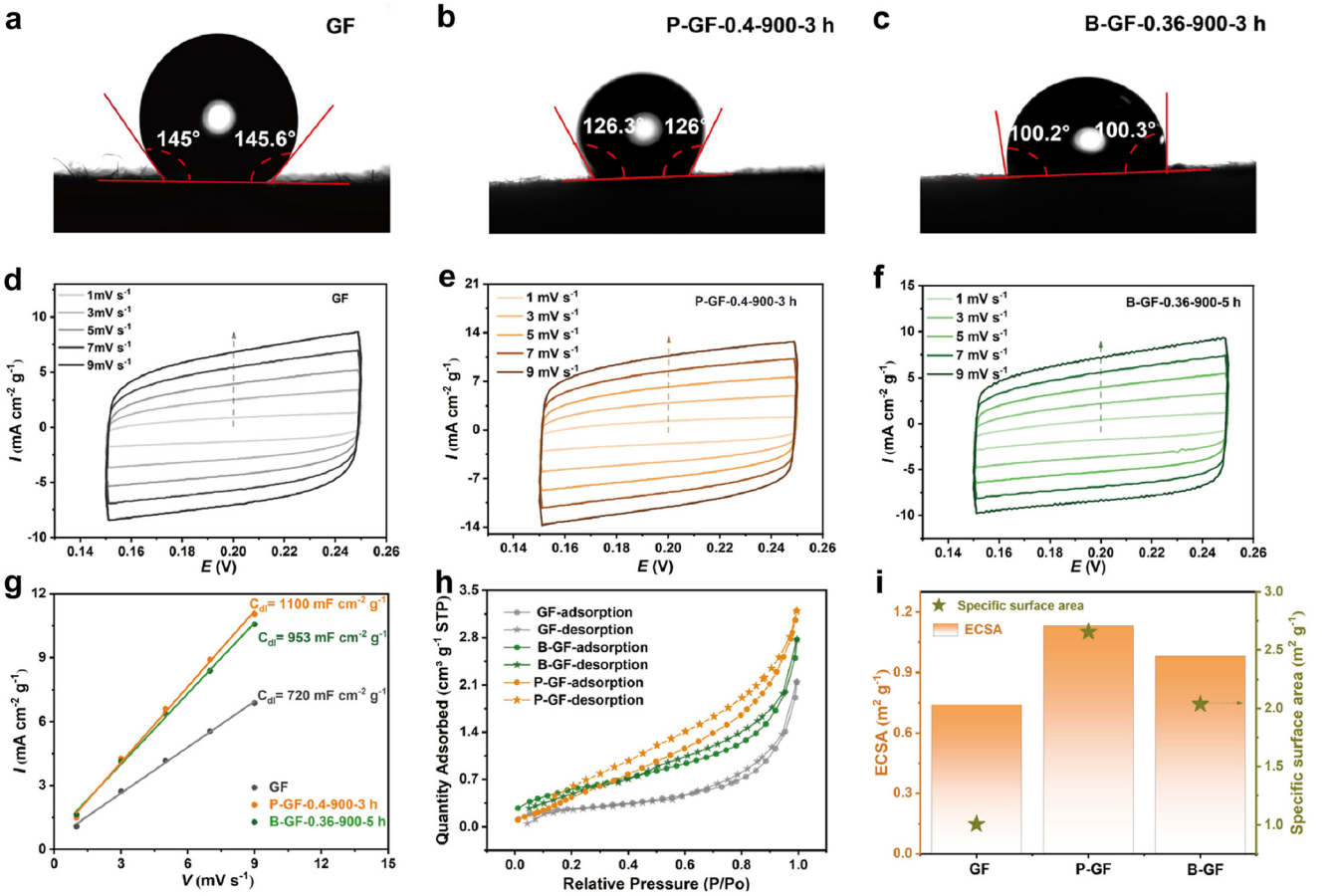

Fig. 3 Contact angle images (a–c), ECSA test results (d–g), adsorption and desorption isotherms (h) and comparison of the ECSA and BET specific surface areas of GF, P–GF, and B–GF (i).

treatment with heteroatom doping, the increase in ECSA is the result of the combined effect of the improvement in hydrophilicity and the BET specific surface area. The aforementioned studies indicated that heteroatomic doping enhances material infiltration and the electrochemical surface area effectively; all of these are the reasons that contribute to its superior electrochemical reaction activity.

Furthermore, the impact of B and P heteroatom doping on the electrical conductivity of the GF electrode was examined (Fig. 4a). The findings indicate that the incorporation of B and P can enhance the conductivity of the GF electrode to some extent, which may be attributed to an increase in carrier concentration and optimization of the electronic structure.[42] The XRD test (Fig. 4b) indicated the characteristic diffraction peaks of the three GF electrodes. The crystal planes of (002) and (100) appeared at approximately 26° and 43°, corresponding to the graphite microcrystalline structure of GF. However, the angle of the crystal plane (002) of the B–GF and P–GF exhibited a slight decrease, and the peak shape has become broader and more rounded, indicating an expansion in the crystal lattice spacing due to the heteroatom doping.[43] In particular for B–GF, due to numerous surface defects, the XRD diffraction peaks become broader and more dispersed. Raman spectroscopy (Fig. 4c) revealed the characteristic D peak (at 1350 cm^{-1}) and G peak (at 1598 cm^{-1}) in the three GF materials; however, the ratio of the D peak to G peak intensity (I_D/I_G) increased significantly following B- and P-doping. The larger I_D/I_G meant the greater degree of defect of the electrode materials. Thus, the introduction of heteroatoms increased the number of surface defects in carbon materials. Specifically, the process of B doping introduced additional defect sites, which in turn enhanced the reaction activity of the relatively less electrochemically active BQDS.

The elemental compositions of the surfaces of various GF electrode materials were investigated using XPS. The total spectra and characteristic fine spectra results for GF, P–GF and B–GF, obtained from XPS tests, are respectively depicted in Fig. 4d–f and Fig. 4g–i. As depicted in Fig. 4d, peaks corresponding to C 1s (~284 eV), N 1s (~400 eV), and O 1s (~532 eV) were observed in the XPS total spectra of both GF and P–GF. Additionally, the P2p peak at 134 eV was also detected in P–GF, indicating the successful introduction of the P element. The content of C, N, O, and P in GF and P–GF-0.4-900-3 h is listed in Table S1. Notably, the content of O in P–GF is significantly higher than that in GF, while the content of P is approximately 1.7%. The results of the XPS

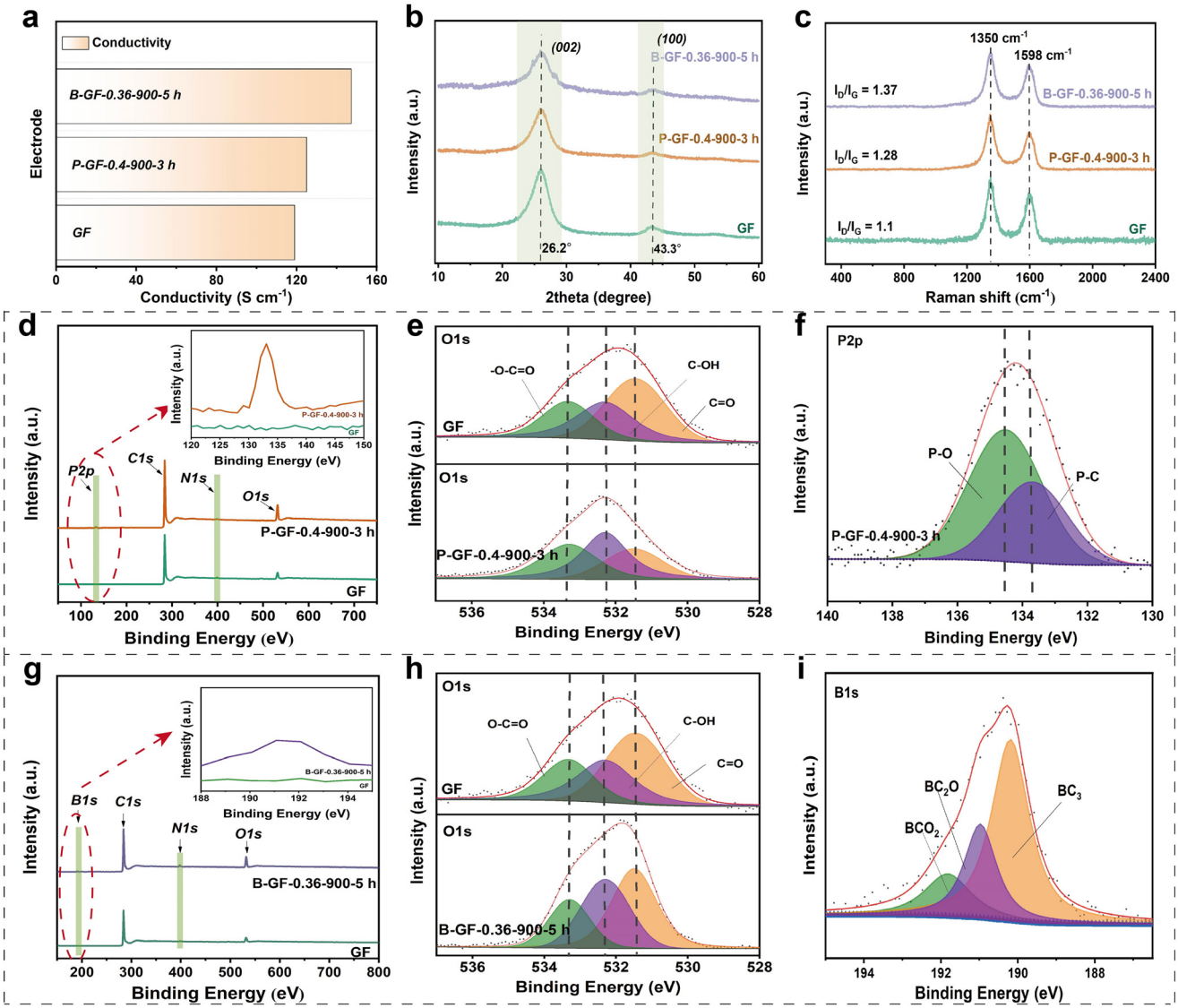

Fig. 4 Conductivity of various heteroatom-doped GF (a); XRD (b) and Raman (c) spectra of P–GF, B–GF, and GF; XPS full spectra and a magnified view of the P2P of P–GF and GF (d); O 1s fine spectra of P–GF and GF (e); P 2p fine spectrum of P–GF (f); XPS full spectra and a magnified view of the B1s of B–GF and GF (g); O 1s fine spectra of B–GF and GF (h); B 1s fine spectrum of B–GF (i).

fine spectrum fitting indicate that the surface of the P–GF electrode material exhibits a relatively higher concentration of –OH groups. The increase in oxygen content is primarily responsible for the enhanced hydrophilicity. P primarily exists in the forms of P–C and P–O, which may act as active adsorption sites for AQSH and facilitate electrochemical reactions.

The XPS total spectra of B–GF and GF are presented in Fig. 4g. In addition to the typical C 1s, N 1s, and O 1s peaks, the B 1s peak is also evident in B–GF-0.36-900-5 h, indicating that boron was successfully introduced into GF. To analyze the changes in functional groups, the fine spectra of O 1s and B 1s are shown in Fig. 4h and i, and the elemental content on the surface of GF and B–GF-0.36-900-5 h is listed in Table S2. The content of hydroxyl and carboxyl groups on the surface of B–GF-0.36-900-5 h has significantly increased compared to that of GF, which is more conducive to enhancing hydrophilicity and the adsorption of vanadium ions. The fine spectra of B 1s reveal that boron consists of BCO_2, BC_2O, and BC_3, indicating successful doping of B in GF, which is crucial for enhancing the catalytic activity and wettability of the electrode.

In this paper, density functional theory (DFT) was utilized to analyze the adsorption activity of GF materials doped with various heteroatoms towards quinone-based active substances. This was achieved by calculating the binding energies of AQSH or $BQDSH_2$ on different graphite-based electrodes. The adsorption process is depicted in Fig. 5a and b, while the adsorption energies are listed in Fig. 5c and d. For AQSH and $BQDSH_2$, the adsorption energy on P–GF and B–GF, respectively, was the lowest, indicating that AQSH/$BQDSH_2$ and P–GF/B–GF had a robust

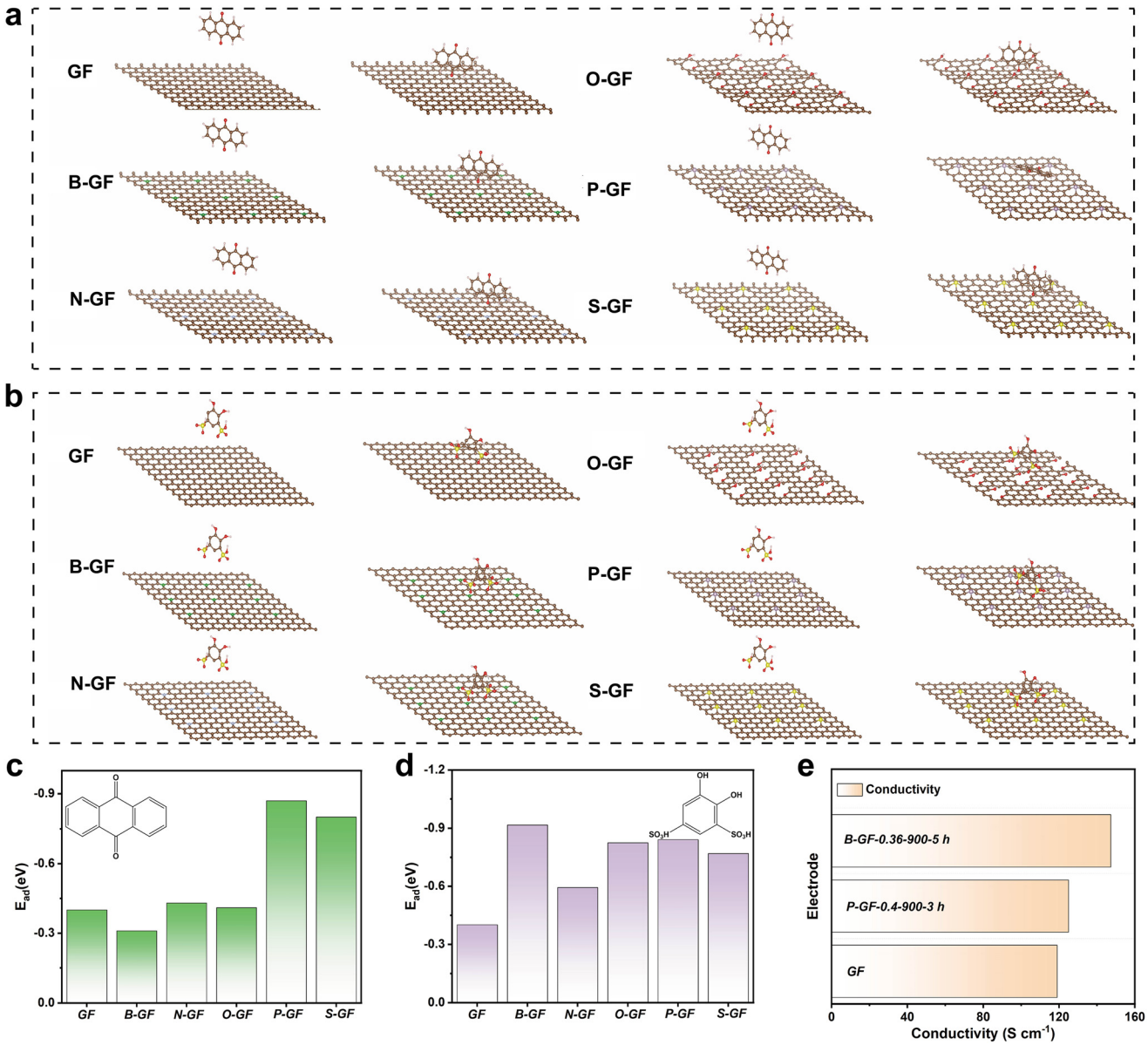

Fig. 5 Adsorption simulation of anthraquinone (a) and benzoquinone (b) on different heteroatom-doped GF electrodes; adsorption energy of anthraquinone (c) and benzoquinone (d) on different heteroatom-doped GF electrodes; conductivity of various heteroatom-doped GFs (e).

interaction. This suggested that P or B doping might enhance the electrochemical reactivity of graphite felts towards anthraquinone and benzoquinone molecules. The simulation results theoretically analyzed the significant reason why specific heteroatom-doped electrode materials substantially improved the electrochemical performance of specific quinone-based electrolytes. Furthermore, the conductivity of various heteroatom-doped graphene foam (GF) measured using the four-probe method is shown in Fig. 5e. Here, the conductivity of P–GF and B–GF surpasses that of the pristine GF and other doped samples. The *in situ* doping of boron and phosphorus can enhance the electrical conductivity of the carbon materials by providing additional electrons and creating external defects, along with a large number of active sites.[44] Coupled with its superior adsorption activity towards specific quinone-based molecules, it demonstrates even better electrochemical activity for AQSH and $BQDSH_2$.

The aforementioned research indicates that P–GF has higher physical and electrochemical specific surface areas than GF, along with excellent electrical conductivity. These properties have led to a significant improvement in the electrochemical performance of AQSH. The electrode B–GF, which possesses excellent hydrophilicity and conductivity, has also enhanced the electrochemical performance of $BQDSH_2$. Additionally, the doping of heteroatoms has regulated the microscopic structural characteristics of graphite materials, thereby influencing the electrochemical activity of the electrode. This was illustrated by DFT calculations.

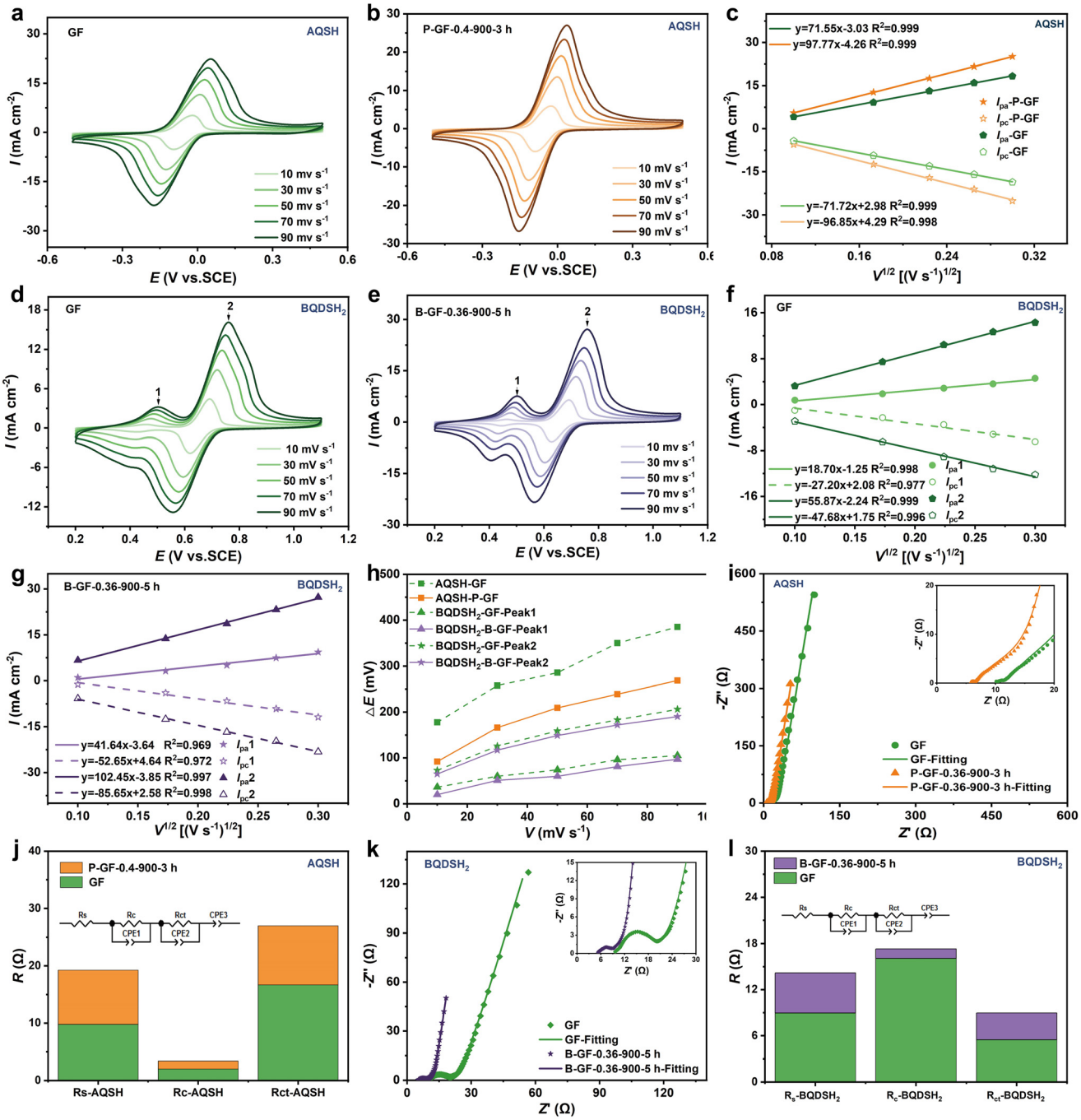

Fig. 6 CV curves of GF (a) and P–GF-0.4-900-3 h (b) in 5 mM AQSH at various scan rates; the relationship between the peak current and the square root of the scan rate (c); CV curves of GF (d) and B–GF-0.36-900-5 h (e) in 5 mM $BQDSH_2$ at different scan rates; the relationship between the peak current and the square root of the scan rate for GF (f) and B–GF-0.36-900-5 h (g); the redox peak position difference of AQSH and $BQDSH_2$ on different electrodes (h); the EIS Nyquist plots and a local magnified view of the high-frequency area of AQSH on GF and P–GF-0.4-900-3 h (i) with the corresponding equivalent circuit (j); the EIS Nyquist plots and a local magnified view of the high-frequency area of $BQDSH_2$ on GF and B–GF-0.36-900-5 h (k) with the corresponding equivalent circuit (l).

Furthermore, the electrochemical kinetics of AQSH/$BQDSH_2$ on P–GF/B–GF were studied in detail using CV tests at various scan rates, as depicted in Fig. 6a and b and Fig. 6d and e. Additionally, linear relationship curves were constructed between the square root of the scan rate and the peak current, as shown in Fig. 6c, f and g. These curves indicated that the electrode reactions were diffusion-controlled. The diffusion coefficients for the oxidation reaction (D_O) and reduction process (D_R), along with the charge-transfer rate constant (k), were calculated using the formulas for a quasi-reversible process (eqn (S3)–(S5)). The results are presented in Table S3. The diffusion coefficient for the electrochemical reaction of AQSH on P–GF was found to be double that on GF, and the charge-transfer rate

constant (k) was quadrupled. This further confirms that the electrochemical kinetics of AQSH are significantly enhanced on P–GF. The CV curves of $BQDSH_2$ on GF/B–GF both exhibited two pairs of redox peaks, corresponding to the two pairs of electron transfer of $BQDSH_2$. The D and k values of $BQDSH_2$ on B–GF were significantly greater than those on GF, particularly the k value of the second peak on B–GF, which was tenfold that on GF. Fig. 6h illustrates the difference in redox peak positions (ΔE) between the two systems without ohmic compensation. The ΔE measured on P–GF/B–GF at the same scan rate was significantly smaller than that on GF, indicating that heteroatom doping enhances the reversibility of the corresponding electrochemical redox reactions.

Furthermore, electrochemical impedance spectroscopy (EIS) tests were conducted on various GF electrodes in AQSH or $BQDSH_2$ electrolytes to investigate their respective electrochemical reaction processes. The Nyquist plots for GF and P–GF in AQSH were obtained at a polarization potential of −0.13 V (Fig. 6i), corresponding to the electrochemical redox reaction potential of AQSH. The plots included two semi-circles in the high-frequency region and a straight line in the low-frequency region, indicating that the electrochemical reaction process is mixed controlled by both electron transfer and mass transport processes. The corresponding equivalent circuit and fitting results are shown in Fig. 6j. The two semicircles represent interface resistance (R_c) and charge transfer resistance (R_{ct}), while the line corresponds to the diffusion resistance. Compared with GF, the R_c value of P–GF decreased significantly, indicating that P–GF is more conducive to the contact between the fibers in the electrode, the electrolyte and the electrode, which is consistent with the result that P–GF possesses a higher ECSA. The lower R_{ct} of P–GF indicated that P–GF exhibited better electrochemical activity for AQSH. The Nyquist plots of $BQDSH_2$ on B–GF at a polarization potential of 0.65 V, along with the corresponding equivalent circuit and fitting results, are shown in Fig. 6k and l. The fitting values for R_s, R_c, and R_{ct} of B–GF decreased significantly compared to those of GF, a result attributed to the enhancement in conductivity and electrochemical activity following B-doping. Consequently, the total resistance of B–GF was much smaller than that of GF. The EIS tests confirmed once again the promoting effect of B–GF and P–GF on the electrochemical reaction kinetics of positive $BQDSH_2$ and negative AQSH.

The physical characterization and electrochemical analysis indicated that B–GF and P–GF exhibited excellent electrochemical performance for $BQDSH_2$ and AQSH electrolytes, respectively, and the preparation process has been optimized. Based on this, 80 mM $BQDSH_2$ (12 mL) and B–GF-0.36-900-5 h were utilized as the positive electrolyte and positive electrode materials, while 80 mM AQSH (12 mL) and P–GF-0.4-900-3 h served as the negative electrolyte and negative electrode material, and 1 M H_2SO_4 solution was used as the supporting electrolyte to assemble an all-quinone aqueous redox flow battery. For comparison, GF was used as both the positive and negative electrodes to assemble another flow battery to verify the effectiveness of the targeted design of electrode materials.

As depicted in Fig. 7a, the charge–discharge curves of the battery with B–GF/P–GF electrodes exhibited a higher discharge voltage plateau and a lower charge voltage plateau. This resulted in reduced polarization overpotential at various current densities and increased charge and discharge

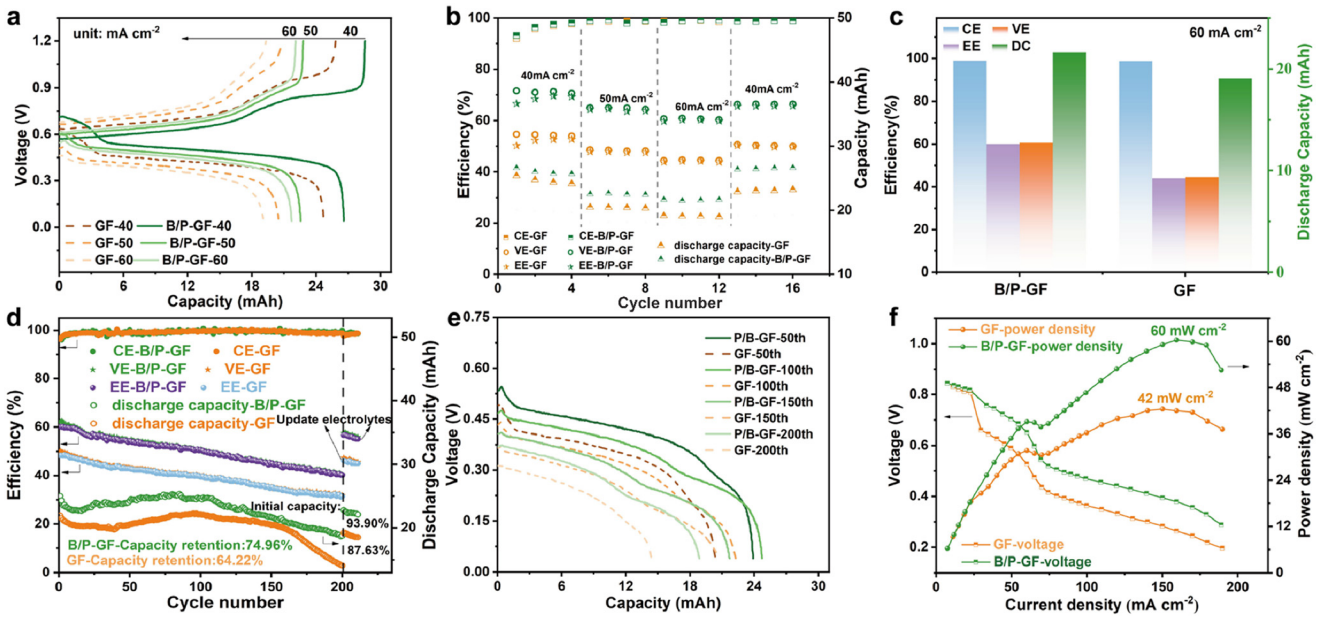

Fig. 7 Charge and discharge curves of the $BQDSH_2$/AQSH AORFB with GF or B/P–GF as electrodes at various current densities (a); efficiencies and discharge capacity of different batteries (b and c); cycle stability test over 200 consecutive charge–discharge cycles (d and e); polarization and power density curves of the battery with GF or B/P–GF as electrodes (f).

capacity. Additionally, the coulombic efficiency (CE), voltage efficiency (VE), and energy efficiency (EE) of the optimized battery were significantly higher than those of the blank group battery (Fig. 7b). Consequently, the batteries in the electrode optimization group exhibited superior rate performance. The battery efficiencies and discharge capacity at 60 mA cm^{-2} of the two groups of batteries are compared in Fig. 7c to analyze the effect of the heteroatom-doped electrodes on the performance of AORFBs more intuitively. The cycling stability at the current density of 50 mA cm^{-2} during 200 charge–discharge cycles is shown in Fig. 7d and e. It can be seen that the efficiencies and discharge capacity of the optimized battery were always higher than those of the contrast battery, and the capacity retention of the former was 74.96%, approximately 10% higher than that of the latter. After the battery has undergone 200 cycles of charging and discharging, the electrolyte is replaced, and the recovery of the battery's performance is examined. By comparing the discharge capacity of the first cycle, it is found that the percentage of the capacity restored after electrolyte updating for the optimized B–GF/P–GF battery was 93.90%, which is significantly higher than that for the GF battery (87.63%). Furthermore, after updating the electrolyte, the battery's efficiency nearly returned to its original level. This also indicates, to some extent, that the degradation of battery performance is primarily due to the deterioration of the electrolyte or the crossover between the positive and negative electrodes. To investigate the primary causes of battery performance degradation, CV tests were conducted on the positive and negative electrolytes before and after the cycle stability test to assess the impact of electrolyte cross-penetration. The results are presented in Fig. S2, which depicts the CV curves of the electrolytes following charge–discharge cycles for the original electrolyte, as well as for the electrolyte in the battery with GF as the electrode and the battery with B/P–GF as the electrode. The findings indicate that no redox peaks of $BQDSH_2$ were observed in any of the three groups of negative AQSH electrolytes, whereas the redox peaks of negative AQSH were detected in the positive $BQDSH_2$ electrolyte. This suggests that the capacity degradation of the battery is primarily due to the transmembrane permeation of negative AQSH into the positive $BQDSH_2$ electrolyte, which significantly affects the electrochemical redox reaction of the positive electrode $BQDSH_2$. Consequently, the battery capacity has undergone a substantial decrease. This necessitates optimization and improvement of both the electrolyte structure and the membrane to further enhance the battery's cycle stability. This also implies that the degradation is less influenced by the electrode materials.

Finally, the discharge polarization curves and the power density curves of the two batteries are presented in Fig. 7f, which are more directly related to the performance of the electrode materials. The composition and surface microstructure of the electrode material directly affect the electrode reaction kinetics and determine the polarization overpotential of the battery. Electrode materials with superior activity tend to result in lower polarization for the corresponding batteries, thereby enabling higher power density. Here, the voltage drop of the B–GF/P–GF battery is observed to be less than that of the GF battery, and the peak power density reaches 60 mW cm^{-2}, which is nearly 1.5 times higher than that of the GF battery (42 mW cm^{-2}). The battery performance test clearly indicates that utilizing B–GF and P–GF as the positive and negative electrodes, respectively, can effectively enhance the performance of quinone-based AORFBs. However, the performance of the battery still needs to be further improved, which requires the collaborative optimization of the active electrolyte, separator and electrode. In this work, we have established a solid foundation for the future research by initially exploring the intrinsic properties of electrode materials that are better suited for quinone-based electrolytes, with the aim of optimizing their application in high-performance aqueous organic redox flow batteries.

3 Conclusions

Utilizing a straightforward and efficient strategy involving the doping of heteroatoms, two varieties of carbon felt electrode materials were identified for their high activity in the electrochemical reactions of the negative AQS^- and the positive $BQDS^{2-}$. The surface properties and electrochemical performances of the corresponding electrode materials were systematically investigated. The results indicated that P–GF exhibited superior electrocatalytic activity for anthraquinone at the negative electrode, whereas B–GF demonstrated enhanced electrocatalytic activity for benzoquinone at the positive electrode. This was attributed to the synergistic effects of the excellent hydrophilicity, conductivity and the strong adsorption capabilities for these quinone based electroactive ions. A BQDS/AQS all-quinone AORFB with B–GF as the positive electrode and P–GF as the negative electrode was assembled. At a current density of 60 mA cm^{-2}, the energy efficiency of this battery can reach 60%. Compared to the battery with both the positive and negative electrodes made of pristine GF, the EE has increased by 18%, and the power density has increased by nearly 43%, which further verifies the effectiveness and necessity of the targeted design of electrode materials in enhancing the performance of AORFBs.

4 Experimental

4.1 Preparation of heteroatom-doped GF

The raw graphite felt required ultrasonic cleaning in a mixture of ethanol and water for 30 minutes to eliminate impurities, followed by drying in a vacuum drying oven at 80 °C for 24 hours. The nitrogen source was obtained by dissolving 0.3 M urea in a 1 : 10 ethanol-to-water mixture (by volume), the sulfur source by dissolving 0.02 M thymol blue in ethanol, the oxygen source with 30% H_2O_2, the phosphorus

source with a 0.08 M HEDP solution (ethanol : water = 1 : 10, by volume), and the boron source with a 0.36 M potassium tetraborate solution. The original GF was subjected to ultrasonic treatment in the specified soaking solution for 30 minutes, followed by drying in a vacuum drying tank at 80 °C for 24 hours. The materials were then calcined in a pipe furnace at 900 °C for 3 hours, with a heating rate of 5 °C per minute. After the heat treatment, P–GF, N–GF, S–GF, and O–GF were washed with water, while B–GF was initially washed with 1 M HCl and subsequently rinsed with water until neutral. They were then dried in a vacuum drying tank at 80 °C for 24 hours. Finally, the finished heteroatom-doped graphite felts were prepared. The preparation process of the heteroatom-doped graphite felts is illustrated in Scheme 1 below.

4.2 Preparation of positive and negative quinone-based electrolytes

To improve the water solubility of quinone-based sulfonates, the sulfonic acid sodium salt was substituted with sulfonate *via* the cation exchange process. The 732 strong acid cation exchange resin (hydrogen type, Macklin) was preconditioned by flushing with 1 M H_2SO_4 (≥98%, Sinopharm Chemical Reagent Co., Ltd.) and then washing with DI-H_2O until the pH of the solution from the outlet of the column reached 7. Then, 100 mL of 8 mM AQSNa (98%, Macklin) or 40 mL of 20 mM $BQDSNa_2$ (97%, Macklin) aqueous solution was introduced into the pretreated columns, respectively, three times to ensure that AQSNa or $BQDSNa_2$ was fully converted into AQSH or $BQDSH_2$.

4.3 Material characterization

Scanning electron microscopy (S4800, Hitachi, Ltd., Tokyo) was used to analyze the surface topography of the materials. X-ray photoelectron spectroscopy (XPS, AXIS UltraDLD, Shimadzu Co., Tokyo) was employed to study the elemental composition and chemical state. X-ray diffraction (XRD, Bruker D8 ADVANCE, Germany) and Raman spectroscopy (Raman, HORIBA Scientific LabRAM HR Evolution) were utilized to analyze the form of carbon in heteroatom-doped electrode materials. A contact angle tester (Theta, JC2000D1, ZhongChen) was used to test the wettability. A conductivity meter was used to measure the conductivity of the materials.

4.4 Electrochemical test

A CHI 760E electrochemical workstation (Shanghai Chenhua, China) was utilized to conduct cycle voltammetry (CV) and electrochemical impedance spectroscopy (EIS) measurements using a conventional three-electrode system. In this setup, the prepared GF served as the working electrode, a saturated calomel electrode was used as the reference electrode, and a Pt sheet electrode (5 mm × 5 mm) functioned as the counter electrode. The electrochemical performance of various heteroatom-doped electrodes was assessed in an electrolyte solution of AQSH or $BQDSH_2$.

4.5 Battery test

An all-quinone-based asymmetric redox flow battery (AORFB) was assembled using a graphite felt (1 cm^2) as both the positive and negative electrodes, Nafion 212 as the diaphragm, AQSH as the negative active electrolyte, $BQDSH_2$ as the positive active electrolyte, and 1 M H_2SO_4 as the supporting electrolyte. The charge–discharge curve was measured using a charge–discharge instrument (CJ2001B, LANHE) at various current densities under N_2 protection. The electrolyte flow rate was maintained at 35 mL per minute with a peristaltic pump (BT100-1L, Longer Pump).

Author contributions

Minghua Jing: formal analysis, investigation, writing – original draft, conceptualization, funding acquisition, project administration, and writing – review & editing. Yanqiu Chen: methodology, writing – original draft, and writing – review & editing. Yuxuan Yang: conceptualization, investigation writing – original draft, and writing – review & editing. Mengnan Zhang: methodology and investigation. Bo Wang: methodology and investigation. Zeyu Xu: formal analysis, investigation and writing – review & editing. Dawei Fang: supervision, funding acquisition, and writing – review & editing.

Conflicts of interest

There are no conflicts to declare.

Data availability

Supplementary information is available. See DOI: **https://doi.org/10.1039/D5IM00204D**.

The data supporting this article have been included in this published article and its SI files.

Acknowledgements

This research was funded by the National Natural Science Foundation of China (No. 22403039; No. 22173039), the Technology Applied Basic Research Program of the Science and Technology Department of Liaoning Province (2025JH2/101330138), the General Project of Science and Technology Department of Liaoning Province (2025-MS-108), the Foundation of Liaoning Province Education Administration (LJKMZ20220445; JYTMS20230760), the 2024 basic research project of Liaoning University (LJKLJ202411), the Liaoning Revitalization Talents Program of Science and Technology Department of Liaoning Province (XLYC2202040) and the Key Technologies R & D Program of Liaoning Provincial Department of Education (LJKZZ20220018).

References

1 Z. Khalid, L. Zhao, E. Elahi and X. Chang, The impact of green management on green innovation in sustainable technology: Moderating roles of executive environmental

awareness, regulations, and ownership, *Environ. Dev. Sustainable*, 2024, DOI: **10.1007/s10668-024-05393-9**.
2 D. Benavides, P. Arévalo, E. Villa-Ávila, J. A. Aguado and F. Jurado, Predictive power fluctuation mitigation in grid-connected PV systems with rapid response to EV charging stations, *J. Energy Storage*, 2024, **86**, 111230.
3 A. Ashok and A. Kumar, A comprehensive review of metal-based redox flow batteries: Progress and perspectives, *Green Chem. Lett. Rev.*, 2024, **17**, 2302834.
4 C. M. Krowne, Physics, electrochemistry, chemistry, and electronics of the vanadium redox flow battery by analyzing all the governing equations, *Phys. Chem. Chem. Phys.*, 2024, **26**, 2823–2862.
5 G. Yang, Y. Zhu, Z. Hao, Q. Zhang, Y. Lu, Z. Yan and J. Chen, An aqueous all-quinone-based redox flow battery employing neutral electrolyte, *Adv. Energy Mater.*, 2024, **14**, 2400022.
6 M. Mansha, A. Ayub, I. A. Khan, S. Ali, A. S. Alzahrani, M. Khan, M. Arshad, A. Rauf and S. Akram Khan, Recent development of electrolytes for aqueous organic redox flow batteries (Aorfbs): Current status, challenges, and prospects, *Chem. Rec.*, 2024, **24**, e202300284.
7 C. M. Davis, C. E. Boronski, T. Yang, T. Liu and Z. Liang, Molecular engineering of redox couples for non-aqueous redox flow batteries, *Batteries*, 2023, **9**, 504.
8 X. Zhang, A. Valencia, W. Li, K. Ao, J. Shi, X. Yue, R. Zhang and W. A. Daoud, Decoupling activation and transport by electron-regulated atomic-Bi harnessed surface-to-pore interface for vanadium redox flow battery, *Adv. Mater.*, 2024, **36**, 2305415.
9 M. Skyllas-Kazacos, Review—Highlights of UNSW all-vanadium redox battery development: 1983 to present, *J. Electrochem. Soc.*, 2022, **169**, 070513.
10 S. Gentil, D. Reynard and H. H. Girault, An organic electroactive material for flow batteries, *Curr. Opin. Electrochem.*, 2020, **21**, 7–13.
11 A. Ramar, F. M. Wang, R. Foeng and R. Hsing, Organic redox flow battery: Are organic redox materials suited to aqueous solvents or organic solvents, *J. Power Sources*, 2023, **558**, 232611.
12 G. Sikukuu Nambafu, Organic molecules as bifunctional electroactive materials for symmetric redox flow batteries: A mini review, *Electrochem. Commun.*, 2021, **127**, 107052.
13 B. Hu, Y. Tang, J. Luo, G. Grove, Y. Guo and T. L. Liu, Improved radical stability of viologen anolytes in aqueous organic redox flow batteries, *Chem. Commun.*, 2018, **54**, 6871–6874.
14 X. Wang, J. Chai, A. Lashgari and J. J. Jiang, Azobenzene-based low-potential anolyte for nonaqueous organic redox flow batteries, *ChemElectroChem*, 2021, **8**, 83–89.
15 C. T. Nie, H. J. Han, Y. H. Li, S. H. Zheng and Y. Wang, Porous graphite felt modified with carbon nanoparticles for an MV/4-HO-TEMPO flow battery, *ACS Appl. Nano Mater.*, 2024, **7**, 9950–9959.
16 T. Yin, J. Duanmu and L. Liu, Viologen-based aqueous organic redox flow batteries: Materials synthesis, properties, and cell performance, *J. Mater. Chem. A*, 2024, **12**, 15519–15540.
17 B. Zhang, B. R. Schrage, A. Frkonja-Kuczin, S. Gaire, I. A. Popov, C. J. Ziegler and A. Boika, Zwitterionic ferrocenes: An approach for redox flow battery (RFB) catholytes, *Inorg. Chem.*, 2022, **61**, 8117–8120.
18 B. Lu, K. Yu, W. Shao, Y. Ji and F. Zhang, Organic redox-active molecules for alkaline aqueous redox flow batteries, *Curr. Opin. Green Sustainable Chem.*, 2024, **47**, 100905.
19 J. Y. Kim, J. W. Ho, D. Kim, M. W. Moon, G. H. Choi and P. J. Yoo, Unveiling dominant impact of electrochemical stability on performance deterioration in alkaline redox flow batteries utilizing different benzoquinone derivatives, *J. Power Sources*, 2024, **611**, 234766.
20 K. Lin, Q. Chen and M. Gerhardt, Alkaline quinone flow battery, *Science*, 2015, **6255**, 1529–1532.
21 B. Huskinson, M. P. Marshak, C. Suh, S. Er, M. R. Gerhardt, C. J. Galvin, X. Chen, A. Aspuru-Guzik, R. G. Gordon and M. J. Aziz, A metal-free organic–inorganic aqueous flow battery, *Nature*, 2014, **505**, 195–198.
22 B. Yang, L. Hoober-Burkhardt, F. Wang, G. K. S. Prakash and S. R. Narayanan, An inexpensive aqueous flow battery for large-scale electrical energy storage based on water-soluble organic redox couples, *J. Electrochem. Soc.*, 2014, **161**, A1371–A1380.
23 S. Zhang, X. Li and D. Chu, An organic electroactive material for flow batteries, *Electrochim. Acta*, 2016, **190**, 737–743.
24 S. H. Park, J. Ha, D. W. Kim, C. Hwang, J. I. Choi, H. S. Park and Y. Kim, Mesoporous graphite felt electrode prepared via thermal oxidative etching on all-vanadium redox flow batteries, *Chem. Eng. J.*, 2024, **500**, 157238.
25 X. Yang, X. Li, T. Xu, H. Cai, C. Zhao, N. Song and P. Ding, Enhanced energy efficiency of aqueous organic redox flow batteries: Carbon-based heterostructure electrodes guided by an interface engineering strategy, *J. Mater. Chem. A*, 2024, **12**, 24459–24467.
26 Y. Zhao, T. Ramachandran, A. Ghosh, A. G. Sehemi, Y. A. Kumar, S. S. Rao, A. K. Yadav and D. Mani, Unlocking the potential of vanadium redox flow batteries: Recent advances in biomass lignin-based carbon fibers and future outlook, *Biomass Bioenergy*, 2025, **200**, 108052.
27 T. Ramachandran, R. Khan, A. Ghosh, M. Hussien, Y. A. Kumar, N. P. Reddy and M. Moniruzzaman, Sustainable carbon electrode materials from biomass for redox flow batteries, *Biomass Bioenergy*, 2025, **198**, 107846.
28 N. Roy, Y. A. Kumar, T. Ramachandran, A. M. Fouda, H. H. Hegazy, M. Moniruzzaman and S. W. Joo, Biomass-derived nanostructures and hydrothermal carbon spheres: A review of electrochemical applications in redox flow battery, *J. Ind. Eng. Chem.*, 2025, **144**, 228–254.
29 S. Wu, X. Lv, Z. Ge, L. Wang, L. Dai and Z. He, Thiourea-grafted graphite felts as positive electrode for vanadium redox flow battery, *Front. Chem.*, 2021, **8**, 626490.
30 J. Y. Kim, Y. C. Kang, W. Ahn, S. A. Song, K. Kim, J. Y. Woo, J. Park and S. N. Lim, Multi-porous electrode derived from zeolitic imidazolate framework-8 coating through

continuous two-stage heat treatment for vanadium redox flow batteries, *J. Energy Storage*, 2024, **86**, 111225.

31 W. Zhang, J. Xi, Z. Li, H. Zhou, L. Liu, Z. Wu and X. Qiu, Electrochemical activation of graphite felt electrode for VO^{2+}/VO_2^+ redox couple application, *Electrochim. Acta*, 2013, **89**, 429–435.

32 M. Y. Lu, W. W. Yang, Z. K. Zhang, Y. J. Yang and Q. Xu, Lead-modified graphite felt electrode with improved VO^{2+}/VO_2^+ electrochemical activity for vanadium redox flow battery, *Electrochim. Acta*, 2022, **428**, 140900.

33 A. M. Demeku, D. M. Kabtamu, G. C. Chen, Y. T. Ou, Z. J. Huang, T. C. Chiang, H. C. Huang and C. H. Wang, Surface electroactive sites of tungstated zirconia catalysts for vanadium redox flow batteries, *ACS Appl. Mater. Interfaces*, 2024, **16**, 7047–7056.

34 X. Chen, C. Wu, Y. Lv, S. Zhang, Y. Jiang, Z. Feng, L. Wang, Y. Wang, J. Zhu, L. Dai and Z. He, Highly active nitrogen-phosphorus co-doped carbon fiber@ graphite felt electrode for high-performance vanadium redox flow battery, *J. Colloid Interface Sci.*, 2025, **677**, 683–691.

35 Y. Jiang, Y. Wang, G. Cheng, Y. Li, L. Dai, J. Zhu, W. Meng, J. Xi, L. Wang and Z. He, Multiple-dimensioned defect engineering for graphite felt electrode of vanadium redox flow battery, *Carbon Energy*, 2024, **6**, e537.

36 H. Li, H. Wang, Y. Xie, Y. Wang, G. Yan, B. Wang and F. Xue, Enhancement of vanadium redox flow battery performance with nitrogen-functionalized graphite felt electrodes etched by K_2FeO_4, *Ionics*, 2023, **29**, 4087–4097.

37 H. R. Jiang, W. Shyy, L. Zeng, R. H. Zhang and T. S. Zhao, Highly efficient and ultra-stable boron-doped graphite felt electrodes for vanadium redox flow batteries, *J. Mater. Chem. A*, 2018, **6**, 13244–13253.

38 S. C. Kim, H. Lim, H. Kim, J. S. Yi and D. Lee, Nitrogen and oxygen dual-doping on carbon electrodes by urea thermolysis and its electrocatalytic significance for vanadium redox flow battery, *Electrochim. Acta*, 2020, **348**, 136286.

39 J. Su, Y. Zhao and J. Xi, Phosphorus-doped carbon nitride as powerful electrocatalyst for high-power vanadium flow battery, *Electrochim. Acta*, 2018, **286**, 22–28.

40 M. Schnucklake, L. Eifert, J. Schneider, R. Zeis and C. Roth, Porous N-and S-doped carbon–carbon composite electrodes by soft-templating for redox flow batteries, *Beilstein J. Nanotechnol.*, 2019, **10**, 1131–1139.

41 Q. Jiang, Y. Ren, Y. Yang, H. Liu, L. Wang, J. Li, L. Dai and Z. He, High-activity and stability graphite felt supported by Fe, N, S co-doped carbon nanofibers derived from bimetal-organic framework for vanadium redox flow battery, *Chem. Eng. J.*, 2023, **460**, 141751.

42 Y. Zheng, K. Chen, K. Jiang, F. Zhang, G. Zhu and H. Xu, Progress of synthetic strategies and properties of heteroatoms-doped (N, P, S, O) carbon materials for supercapacitors, *J. Energy Storage*, 2022, **56**, 105995.

43 A. Damjanovic, A. Dey and J. O. Bockris, Kinetics of oxygen evolution and dissolution on platinum electrodes, *Electrochim. Acta*, 1966, **11**, 791–814.

44 L. Wang, Y. Wang, M. Wu, Z. Wei, C. Cui, M. Mao, J. Zhang, X. Han, Q. Liu and J. Ma, Nitrogen, fluorine, and boron ternary doped carbon fibers as cathode electrocatalysts for zinc–air batteries, *Small*, 2018, **14**, 1800737.